

Manipulating the Architecture of Atomically Thin Transition Metal (Hydr)oxides for Enhanced Oxygen Evolution Catalysis

Yuhai Dou,^{†,‡} Lei Zhang,^{†,‡} Jiantie Xu,[†] Chun-Ting He,[‡] Xun Xu,[†] Ziqi Sun,[§] Ting Liao,[§] Balázs Nagy,[‡] Porun Liu,^{,‡} and Shi Xue Dou^{*,†}*

[†]Institute for Superconducting and Electronic Materials, Australian Institute for Innovative Materials, University of Wollongong, Wollongong, New South Wales 2500, Australia

[‡]Centre for Clean Environment and Energy, Gold Coast Campus, Griffith University, Gold Coast, Queensland 4222, Australia

[§]School of Chemistry, Physics and Mechanical Engineering, Queensland University of Technology, Brisbane, Queensland 4000, Australia

Corresponding author e-mails: p.liu@griffith.edu.au; shi@uow.edu.au.

ABSTRACT: Graphene-like nanomaterials have received tremendous research interest due to their atomic thickness and fascinating properties. Previous studies mainly focus on the modulation of their electronic structures, which undoubtedly optimizes the electronic properties, but is not the only determinant of performance in practical applications. Herein, we propose a generalized strategy to incrementally manipulate the architectures of several atomically thin transition metal (hydr)oxides, and

study their effects on catalytic water oxidation. The results demonstrate the obvious superiority of a wrinkled nanosheet architecture in both catalytic activity and durability. For instance, wrinkled Ni(OH)₂ nanosheets display a low overpotential of 358.2 mV at 10 mA cm⁻², a high current density of 187.2 mA cm⁻² at 500 mV, a small Tafel slope of 54.4 mV dec⁻¹, and excellent long-term durability with gradually optimized performance, significantly outperforming other nanosheet architectures and previously reported catalysts. The outstanding catalytic performance is mainly attributable to the 3D porous network structure constructed by wrinkled nanosheets, which not only provides sufficient contact between electrode materials and current collector, but also offers highly accessible channels for facile electrolyte diffusion and efficient O₂ escape. Our study provides a perspective on improving the performance of graphene-like nanomaterials in a wide range of practical applications.

KEYWORDS: atomically thin, nanosheets, architecture, oxygen evolution reaction, catalysis

The successful fabrication and use of graphene has stimulated extensive exploration of atomically thin two-dimensional (2D) nanomaterials for both fundamental studies and practical applications.¹⁻⁵ To date, many atomically thin 2D nanomaterials, such as hexagonal boron nitride,^{6,7} graphitic carbon nitride,^{8,9} black phosphorous,^{10,11} layered double hydroxides,^{12,13} transition metal dichalcogenides,^{14,15} metal-organic frameworks,^{16,17} covalent-organic frameworks,^{18,19} and MXenes,^{20,21} have been successfully developed by liquid exfoliation or wet-chemical synthesis.²²⁻²⁵ These nanomaterials with atomic/molecular thickness possess large specific surface areas, exotic electronic properties, excellent mechanical flexibility, and high optical transparency, and consequently they are promising for applications in sensors, energy conversion and storage, biomedicine, (opto)electronics, *etc.*^{14,26-28} With the purpose of further improving their performance, considerable attention has been devoted to the rational design of nanostructures with the desired physical and chemical properties,²⁹ *via* thickness

control,^{30,31} pit/pore creation,^{32,33} vacancy engineering,^{34,35} elemental doping,^{36,37} or heterostructure construction.^{38,39} The modification of nanostructures highlights the future research directions of atomically thin nanomaterials, which are believed to offer great opportunities and challenges for solid state nanochemistry.

Despite the significant progress that has been made in the development of atomically thin nanomaterials, previous works are mainly focused on the modulation and optimization of the surface electronic structures,^{25,27,40-42} which undoubtedly improves their physical and chemical properties, but is not the only determinant of performance in practical applications. The assembled architecture of the nanosheets also plays an important role due to its strong correlation with the optoelectronic, electrical, magnetic, and thermal properties of nanosheet-based devices.⁴³⁻⁴⁵ To date, very few studies have reported the effect of assembled architecture on electrochemical performance, since the rational control of the composition and morphology is very difficult to achieve. It is, therefore, highly desirable but also extremely challenging to develop a universal method to gradually manipulate the architecture of nanosheets with the goal of further improving their properties and functionalities in practical applications.

In this work, we introduced a generalized strategy to incrementally manipulate the architecture of several atomically thin transition metal (hydr)oxides, including Ni(OH)₂, Co(OH)₂ and Mn₃O₄/Mn₂O₃, by finely adjusting the precursor hydrolysis rate and the solution viscosity and polarity. The nanosheet architecture evolves from large agglomerates to small nanoflowers, to large nanoflowers, to wrinkled nanosheets, and finally to flat nanosheets. The electrocatalytic performance of these architectures in the oxygen evolution reaction (OER) was then evaluated, and the results demonstrate the obvious superiority of the wrinkled nanosheet architecture in terms of both catalytic activity and durability over other nanosheet architectures. The 3D porous network structure of the electrode constructed by the

wrinkled nanosheets is the most likely cause of the outstanding OER catalytic performance, because it not only offers large effective surface area for sufficient electrode-material/current-collector contact, but also provides highly accessible channels for facile electrolyte diffusion and efficient mass transfer (*e.g.*, O₂ escape).

RESULTS AND DISCUSSION

In our previous work, a bottom-up self-assembly approach was developed to synthesize a variety of atomically thin nanomaterials (Figure S1), in which H₂O enables the hydrolysis of metal ions, polyethylene-oxide–polypropylene-oxide–polyethylene-oxide (Pluronic P123) forms inverse lamellar micelles and directs the assembly of hydrated precursor oligomers along the 2D confined space, ethylene glycol (EG) assists the formation of lamellar phase for P123 and stabilizes the generated 2D nanocrystals, and hexamethylenetetramine (HMTA) homogeneously releases OH[−] ions to control the hydrolysis of metal ions at an appropriate rate.⁴⁶ Each chemical plays a crucial and irreplaceable role in the synthesis of atomically thin nanomaterials. Even though this approach is effective for preparing various primary ultrathin nanosheets, it is unable to control their aggregate architectures, which have a big influence on their practical performances.

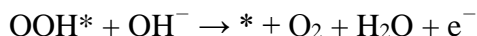
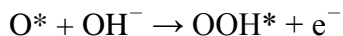
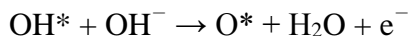
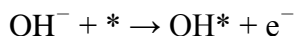
Herein, we propose a generalized manipulation strategy based on our previous synthetic method to make incremental changes in the assembled architectures of various atomically thin nanosheets. Our concept is to rationally adjust the hydrolysis rate of the metal precursor and the polarity of the solvent by finely tuning the volume ratio of H₂O to EG, which results in different aggregation behaviors of the generated nanosheets. As illustrated in Figure 1a, with an increasing H₂O/EG ratio, the aggregate architecture evolves from large agglomerates (designated as 2DXLA, where 2D = two-dimensional, LA = large agglomerates, and X varies depending on the transition metal elements, which is N for nickel, C

for cobalt, and M for manganese) to small nanoflowers (2DXSF), to large nanoflowers (2DXLF), to wrinkled nanosheets (2DXWS), and finally to flat nanosheets (2DXFS). Through this manipulation strategy, a variety of atomically thin nanomaterials with controllable architectures, including Ni(OH)₂, Co(OH)₂, and Mn₃O₄/Mn₂O₃, have been successfully prepared (see Experimental Section and Table S1 for details). The structural features of these architectures were studied by scanning electron microscope (SEM) and transmission electron microscope (TEM). As shown in Figure 1b-d, all architectures are assembled from nanosheet building blocks, which possess atomic thicknesses of 2.0, 1.2, and 2.4 nm for Ni(OH)₂, Co(OH)₂, and Mn₃O₄/Mn₂O₃, respectively (Figure S2). The evolution of the architecture is consistent with the mechanism proposed in Figure 1a, where the size of primary nanosheets increases while the degree of aggregation decreases with increasing H₂O/EG ratio. The changes in nanosheet architecture should be attributed to the variations in the hydrolysis rate of the precursor and the polarity of the solvent. On the one hand, high H₂O addition stimulates rapid hydrolysis and fast condensation of metal precursors during the hydrothermal process,⁴⁷ which consequently lead to the formation of primary nanosheets with large lateral sizes and architectures with a low degree of aggregation. In contrast, high EG content retards the hydrolysis rate of metal precursor by isolating precursor molecules from water phase,⁴⁷ so that nanosheets with small lateral size are produced and they tend to aggregate tightly so as to minimize their surface energy. On the other hand, as H₂O has a higher polarity compared with EG, the polarity of the mixed solvent increases with an increasing H₂O/EG ratio. The increased solvent polarity helps to stabilize the primary nanosheets through the inter-molecular hydrogen bonds,⁴⁸ and therefore, the nanosheets become well dispersed and their aggregation is gradually relieved with the increasing H₂O/EG ratio.

The phase structures of different nanosheet architectures were characterized by X-ray diffraction (XRD), high resolution TEM (HRTEM), and selected area electron diffraction (SAED). As shown in

Figure 2, the evolution of the nanosheet architecture is accompanied by changes in the crystal structure. For $\text{Ni}(\text{OH})_2$, the diffraction peaks of 2DNLA and 2DNSF match well with β - and α - $\text{Ni}(\text{OH})_2$ mixed phase, while those of 2DNLF, 2DNWS and 2DNFS correspond to pure α - $\text{Ni}(\text{OH})_2$ phase (Figure 2a).⁴⁹ β - $\text{Ni}(\text{OH})_2$, with an interlayer distance of ~ 4.37 Å (Table S2), has a compact and hexagonal layered structure that does not permit intercalation of any guest species, while α - $\text{Ni}(\text{OH})_2$, with a much larger interlayer distance of ~ 7.65 Å (Table S2), allows the intercalation of H_2O and anions (*e.g.*, CH_3COO^-) into the interlayer gallery.⁵⁰ As a result, the formation of different phases is mainly attributable to different H_2O additions in precursor solutions. The diffraction peaks of the α - $\text{Ni}(\text{OH})_2$ (003) and (006) planes shift to lower angles, further suggesting the intercalation of guest species and the expansion of interlamellar spacing (from 7.44 to 7.80 Å for d_{003} , Table S2). In addition, the intercalated species also result in poor crystallinity and turbostratic structure of α - $\text{Ni}(\text{OH})_2$ as observed by the significantly decreased peak intensity of the (003) planes. The diffraction patterns of $\text{Co}(\text{OH})_2$ suggest the formation of β - and α - $\text{Co}(\text{OH})_2$ mixed phase for 2DCLA, and pure α - $\text{Co}(\text{OH})_2$ phase for 2DCSF, 2DCLF, 2DCWS, and 2DCFS (Figure 2b).⁵¹ The peak intensity and shift of α - $\text{Co}(\text{OH})_2$ show similar trends to those of α - $\text{Ni}(\text{OH})_2$ for the same reasons explained above. Unlike the relatively stable $\text{Ni}(\text{OH})_2$ and $\text{Co}(\text{OH})_2$, $\text{Mn}(\text{OH})_2$ is easily oxidized by dissolved oxygen in the solvent, which leads to a mixed phase of Mn_3O_4 and Mn_2O_3 (Figure 2c).^{52,53} The HRTEM images and SAED patterns of $\text{Ni}(\text{OH})_2$ samples demonstrate the formation of β/γ - NiOOH in 2DNLA and γ - NiOOH in 2DNWS, which may originate from the electron-beam-induced crystallization of β/α - $\text{Ni}(\text{OH})_2$ and α - $\text{Ni}(\text{OH})_2$, respectively (Figure 2d).⁵⁴ This is further supported by the observed oxidation states of β/γ - CoOOH and γ - CoOOH in 2DCLA and 2DCWS, respectively (Figure 2e). Generally, the HRTEM images and SAED patterns of 2DXLA and 2DXWS are consistent with the XRD results, both of which suggest the changes in the phase structure for different nanosheet architectures (Figure 2d-f).

To study the effect of aggregate architecture on the performance in practical applications, Ni(OH)₂ was first taken as an example, and its OER catalytic properties were evaluated by rotating disk electrode (RDE) measurements in alkaline media (Figure 3). In order to figure out the active species for OER catalysis, cyclic voltammetry (CV) was first conducted at a scan rate of 5 mV s⁻¹ in the voltage range of 1.22–1.72 V vs. reversible hydrogen electrode (RHE). As shown in Figure 3a, a pair of quasi-reversible redox peaks appear at ~1.42 V in the anodic scan and ~1.28 V in the cathodic scan, which represent the oxidation of Ni(II) to Ni(III/IV) and the successive reduction back to Ni(II), respectively. The corresponding reactions can be expressed as Ni(OH)₂ + OH⁻ ↔ NiOOH + H₂O + e⁻.⁵⁵ The oxygen evolution starts at a potential well above that of the anodic peak, and therefore, the NiOOH phase formed *in situ* is believed to be the active species for OER catalysis. In alkaline medium, the proposed catalytic mechanism for the 4-electron transfer OER (4OH⁻ → 2H₂O + O₂ + 4e⁻) can be depicted by the following reaction pathways:⁵⁶



where * represents a Ni active site, and OH*, O* and OOH* are reaction intermediates. It was reported that the NiOOH phase, with an average oxidation state of 3.6 under OER potential, can facilitate the formation of OOH* intermediates (rate-determining step in OER) and the final release of O₂, which consequently enhances the catalytic activity.^{49,57,58} As 2DNWS displays stronger anodic peak when compared with the other architectures, it is expected to provide more active sites and exhibit higher activity towards OER catalysis.

The catalytic activity of different nanosheet architectures was then systematically evaluated by

linear sweep voltammetry (LSV) at 5 mV s^{-1} in the voltage range of 1.22–1.92 V *vs.* RHE. The polarization curves in Figure 3b show that the catalytic activity first increases to a peak value and then decreases dramatically with the evolution of the nanosheet architecture. More specifically, to reach a current density of 10 mA cm^{-2} , the required overpotentials (η , averaged from ten measurements) for 2DNLA, 2DNSF, 2DNLF, 2DNWS, and 2DNFS are 381.8, 381.5, 368.3, 358.2, and 371.6 mV, respectively (Figure 3c), and at $\eta = 500 \text{ mV}$, the recorded current densities are 75.3, 92.3, 153.0, 187.2, and 76.3 mA cm^{-2} , respectively (Figure 3d). In addition, the apparent turnover frequency (TOF) of 2DNWS at η of 500 mV is calculated to be 0.294 s^{-1} , which dramatically exceeds those of 0.118, 0.145, 0.240, and 0.120 s^{-1} for 2DNLA, 2DNSF, 2DNLF, and 2DNFS, respectively. As a result, 2DNWS with a wrinkled-nanosheet architecture exhibits the highest catalytic activity among all the nanosheet architectures. To further confirm the superior catalytic performance of 2DNWS, Tafel plots of the polarization curves were constructed in the low overpotential range. As shown in Figure 3f, the Tafel slopes of 2DNLA, 2DNSF, 2DNLF, and 2DNFS are 65.6, 63.5, 59.0, and 79.5 mV dec^{-1} , respectively, while it is decreased to 54.4 mV dec^{-1} for 2DNWS, indicating the enhanced kinetics of the wrinkled-nanosheet architecture to drive water oxidation.^{59,60} It is also noteworthy that, owing to the atomic thickness and special nanostructure architecture, 2DNWS is among the most efficient $\text{Ni}(\text{OH})_2$ catalysts (without defect creation, elemental doping, heterostructure construction, *etc.*) that have ever been reported (Figure S3).

Durability is another essential criterion to evaluate the catalytic performance of a catalyst.⁶¹⁻⁶³ Here, the durability of different electrodes was evaluated by performing chronopotentiometric test at a constant current density of 10 mA cm^{-2} for 12 h. As can be seen in Figure 3g, different nanosheet architectures result in obvious differences in catalytic stability. The overpotential of 2DNWS decreases initially in the first 1 h and then remains nearly constant with prolonging the reaction time. 2DNSF and

2DNLF show a similar trend in overpotential at the beginning, while they experience a slight increase in the following hours. The increased catalytic activity of 2DNWS, 2DNSF and 2DNLF at the beginning should be attributed to the activation of the catalyst with an increased number of active species participating in the catalytic reaction.^{49,64} By contrast, 2DNLA and 2DNFS exhibit a direct increase in overpotential at the beginning and then suffer from a gradual decline in catalytic activity during the 12 h chronopotentiometric measurement. The Tafel plots for these electrodes after 1 h and 12 h durability tests were constructed, which are consistent with the results of the chronopotentiometric test and further indicate the importance of the nanosheet architecture in determining the catalytic performance (Figure S4).

We further evaluated the OER catalytic performance of $\text{Co}(\text{OH})_2$ under the same test conditions. As shown in Figure S5, the catalytic activity of $\text{Co}(\text{OH})_2$ first increases and then decreases, with 2DCWS reaching the peak value, and the durability tests display similar trends to those of $\text{Ni}(\text{OH})_2$, further confirming the vital role played by the nanosheet architecture in both the catalytic activity and durability.

It is interesting that the evolution of the nanosheet architecture results in obvious changes in catalytic activity when considering the similar specific surface areas (Figure S6). The changes are firstly attributable to different phase structures of the nanosheets. As is well known, before OER catalysis, $\alpha\text{-Ni}(\text{OH})_2$ and $\beta\text{-Ni}(\text{OH})_2$ are oxidized to catalytically active $\gamma\text{-NiOOH}$ and $\beta\text{-NiOOH}$, respectively (Figure S7).⁶⁵ $\gamma\text{-NiOOH}$ differs from $\beta\text{-NiOOH}$ in that it allows the intercalation of various guest species and thus possesses a much larger interlayer spacing (7 Å compared with 4.8 Å).^{55,66} As the interlayer spacing increases with the evolution of the architecture, the catalytic activity is gradually improved due to the facile diffusion and transfer of H_2O , OH^- and O_2 within the interlayer gallery. In addition, the $\gamma\text{-NiOOH}$ with poor crystallization possess numerous defect sites, such as vacancies, edges, corners,

stacking faults, *etc.*, which could serve as highly active species for enhanced OER catalysis.⁶⁷

Nevertheless, we believe that the architecture of the nanosheets plays a much more important role in determining the catalytic activity and durability, especially when comparing the performances of 2DNWS and 2DNFS, where 2DNFS with larger interlayer spacing and more disordered structure exhibits visibly deteriorated catalytic activity compared with 2DNWS. As is well known, apart from the inherent catalytic activity, two external conditions need to be satisfied in order to further improve the catalytic performance, which include intimate electronic contact between the electrode material and the current collector, and high accessibility of the electrode film to the electrolyte, reactants, and products. The 2DNWS electrode, with wrinkled nanosheets integrated into a 3D porous network structure, not only offers a large effective surface area for sufficient electrode-material/current-collector contact, but also provides highly accessible channels for facile electrolyte diffusion and efficient mass transfer, especially the escape of O₂ (Figure 4a and b). By contrast, even though the architectures of 2DNLA, 2DNSF, and 2DNLF allow easy escape of O₂, the limited electronic contact with the current collector severely impedes the catalytic process. In particular, the easy detachment of 2DNLA from the current collector under the rotating shear force and a consequent loss of electronic contact lead to the gradual increase in overpotential and decrease in catalytic activity during the long-term chronopotentiometric test. 2DNFS has sufficient electronic contact with the current collector, while the closely stacked electrode film not only hinders the diffusion of electrolyte, but also blocks the escape of O₂. As a result, small O₂ bubbles are confined inside the electrode film initially, and then aggregate into large ones, which isolate the catalyst surface from the electrolyte and cause dramatic declines in catalytic activity and durability (Figure 4b). The importance of the nanosheet architecture in catalytic activity could also be reflected by the electrochemical surface area (ECSA). The ECSA was estimated from the electrochemical double-layer capacitance (C_{dl}), which is half the value of the linear slope (capacitive current *vs.* scan rate). As

can be seen in Figure S8, 2DNWS exhibits the largest C_{dl} of 3.86 μF compared with those of the other catalysts (1.43 μF for 2DNLA, 1.86 μF for 2DNSF, 2.88 μF for 2DNLF, and 1.02 μF for 2DNFS) due to an optimized combination of sufficient electrode-material/current-collector contact and high ion accessibility. To further confirm our proposed mechanism, the morphology of the nanosheet architectures was examined after 12 h of chronopotentiometric testing. As shown in Figure S9, even though there was slight aggregation in the electrodes, the individual architectures of 2DNLA, 2DNSF, 2DNLF and 2DNWS can still be identified, which indicates that the porous structure of the electrodes still remains with high accessibility to the electrolyte. In comparison, the nanosheets of 2DNFS were severely stacked, and thus cannot provide highly accessible pores/channels for efficient electrolyte diffusion and mass transfer throughout the chronopotentiometric test. Electrochemical impedance spectroscopy (EIS) was also performed after the durability test to evaluate the catalytic kinetics of different architectures. As shown in Figure S10, the Nyquist plots of different catalysts present a compressed semicircle in the high-frequency region and a clear inclined tail in the low-frequency region, in which the high-frequency intercept represents the solution resistance and the electrode-material/current-collector contact resistance, the diameter of the semicircle stands for the charge transfer resistance, and the slope of the tail reflects the diffusion properties.⁶⁸ The relatively large internal and charge transfer resistances of 2DNLA, 2DNSF and 2DNLF result from the insufficient electronic contact between the electrode and the current collector, and the large resistances and low inclination angle of the tail for 2DNFS should be ascribed to the O_2 bubbles confined in the closely stacked nanosheets, which impede the diffusion of electrolyte throughout the electrode film. Generally, 2DNWS exhibits much smaller internal and charge transfer resistances, as well as a favorable inclination angle of the tail, suggestive of efficient electrolyte diffusion, facile mass transfer, and enhanced catalytic kinetics with low energy barriers.

CONCLUSIONS

In summary, a generalized synthetic strategy was developed to manipulate the architecture of atomically thin transition metal (hydr)oxide nanosheets, and the OER catalytic properties were evaluated to recognize the importance of the architecture for practical applications. We found that the wrinkled nanosheets exhibit the best catalytic activity and durability, which is mainly attributable to the sufficient electrode-material/current-collector contact, efficient electrolyte diffusion, and easy O₂ escape provided by the 3D porous network structure. This study is of great significance for optimizing the performances of atomically thin nanomaterials by developing desired architectures with fascinating properties and functionalities for a wide range of practical applications.

METHODS

Generalized strategy for manipulating the architecture of atomically thin transition metal (hydr)oxides: For the synthesis of atomically thin nanosheets, 0.2 g Pluronic P123 was first dissolved in 3.0 g ethanol or acetone under magnetic stirring. A mixed solvent of EG and H₂O was then added to create the oil-water-surfactant equilibrium system. After that, the appropriate metal salt and HMTA were added under vigorous stirring for 30 min, followed by static aging for 24 h. Finally, the precursor solution was transferred into a 45 ml autoclave for hydrothermal synthesis. The reactions were carried out at 150, 160, and 150 °C for 10, 15, and 5 h for nickel, cobalt, and manganese (hydr)oxides, respectively, and different nanosheet architectures were produced by finely adjusting the volume ratio of H₂O to EG. The detailed compositions of the precursor solutions for different nanosheet architectures can be found in Table S1.

Characterizations: The morphology of different types of nanosheet architecture was observed using SEM (JSM-7500FA, JEOL, Tokyo, Japan) and TEM (JEM-2011F, JEOL, Tokyo, Japan) imagings. The

thickness of the nanosheets was determined by observing their edge configurations *via* HRTEM. XRD (MMA, GBC Scientific Equipment LLC, Hampshire, IL, USA), HRTEM, and SAED were employed to identify the phase structures of the atomically thin nanosheets. The specific surface areas were calculated from N₂ adsorption/desorption isotherms using the Brunauer-Emmett-Teller (BET) equation (Micromeritics TriStar II 3020). Before measurements, the powders were degassed under high vacuum at 120 °C for 8 h.

Electrochemical measurements: The catalytic performance of different nanosheet architectures were evaluated by CV and LSV with a rotating-disk electrode (RDE, glassy carbon disk) connected to a VMP3 Multi-channel potentiostat (Biologic Science Instruments). O₂-saturated 1 M KOH (90%, Sigma-Aldrich, for CV and LSV tests) or NaOH ($\geq 98\%$, Sigma-Aldrich, for durability tests) were used as the electrolyte, platinum plate as the counter electrode, and Ag/AgCl (Saturated KCl) as the reference electrode. Before testing, the reference electrode was calibrated against another unused Ag/AgCl electrode stored in saturated KCl solution. For the preparation of the working electrode, 2 mg catalyst was dispersed into 1 ml of a water-isopropanol mixed solution (3:1, v/v) with 25 μ l Nafion[®] solution (5 wt.%, Sigma-Aldrich), and ultrasonicated for 3 min to give a homogeneous suspension. After that, 15 μ l of the catalyst suspension was deposited onto the glassy carbon electrode (loading of ~ 0.15 mg cm⁻²) and finally dried at 80 °C. CV was carried out at a sweep rate of 5 mV s⁻¹ in the voltage range of 0.2–0.7 V *vs.* Ag/AgCl, and LSV was performed at 5 mV s⁻¹ in the range of 0.2–0.9 V *vs.* Ag/AgCl under continuous rotation at 1600 rpm. ECSA was determined from the double-layer capacitance, which was measured by the scan-rate dependence (10, 20, 30, 40, 50, 60 mV s⁻¹) of CVs (0.2–0.3 V *vs.* Ag/AgCl). Repeated tests were carried out and the reported η , current density, TOF, and ECSA were averaged from ten measurements by eliminating the maximum and minimum values. For the durability test, chronopotentiometric responses were recorded at a constant current density of 10 mA cm⁻² for 12 h. EIS

measurement after durability test was performed at 0.5 V *vs.* Ag/AgCl with an amplitude of 10 mV between 200 kHz and 100 mHz.

CV and LSV curves recorded in this study were corrected with 90% *iR*-compensation, and all potentials were calibrated with respect to reversible hydrogen electrode (RHE), using the equation $E_{\text{RHE}} = E_{\text{Ag/AgCl}} + 0.197 + 0.059 \times \text{pH}$, where E_{RHE} is the potential with respect to RHE, and $E_{\text{Ag/AgCl}}$ is the measured potential *versus* the Ag/AgCl reference. Tafel plots were derived from the LSV curves by plotting potential against log(current density). The turnover frequency (TOF) values were calculated based on the following equation: $\text{TOF} = jS/4Fn$, where j (mA cm⁻²) is the current density at an overpotential of 500 mV, S is the surface area of glassy carbon disk, F is the Faraday constant (96485 C mol⁻¹), and n is the number of moles of the metal atoms.

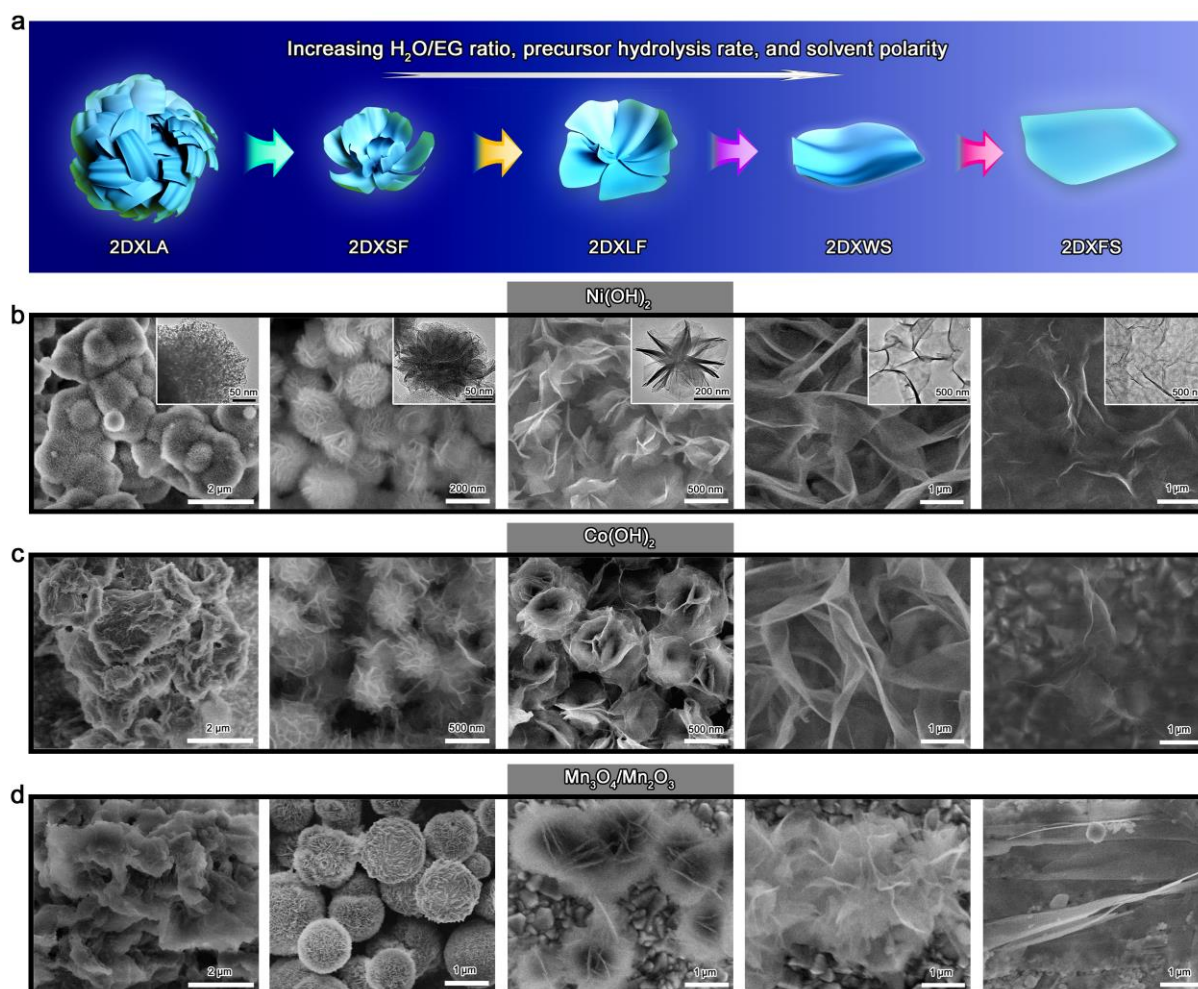


Figure 1. Manipulation of the architecture for atomically thin transition metal (hydr)oxides. (a) Schematic illustration showing the evolution of nanosheet architecture with increasing precursor hydrolysis rate and solvent polarity. (b) Architecture evolution of atomically thin Ni(OH)₂ nanosheets, with insets clearly displaying the changes in the assembled structures. (c) Architecture evolution of atomically thin Co(OH)₂ nanosheets. (d) Architecture evolution of atomically thin Mn₃O₄/Mn₂O₃ nanosheets.

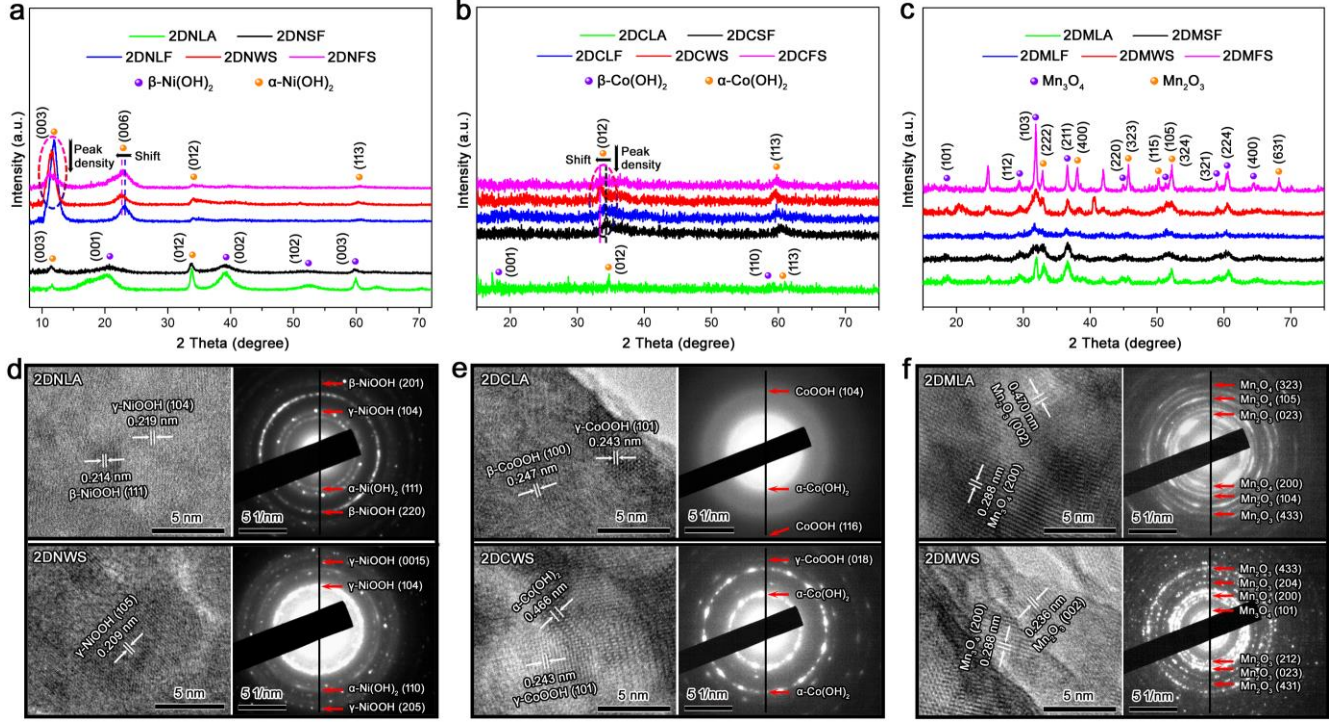


Figure 2. Phase structures of atomically thin transition metal (hydr)oxides with different architectures. (a) XRD patterns showing the mixed β -/ α -Ni(OH)₂ phases of 2DNLA and 2DNSF, and pure α -Ni(OH)₂ phase of 2DNLF, 2DNWS, and 2DNFS. (b) XRD spectra showing the mixed β -/ α -Co(OH)₂ phases of 2DCLA and 2DCSF, and pure α -Co(OH)₂ phase of 2DCLF, 2DCWS, and 2DCFS. (c) XRD spectra showing the mixed Mn₃O₄/Mn₂O₃ phases of different nanosheet architectures. (d-f) HRTEM images and SAED patterns of 2DXLA and 2DXWS, in which Ni(OH)₂ (d) and Co(OH)₂ (e) undergo phase transformations under electron beam radiation.

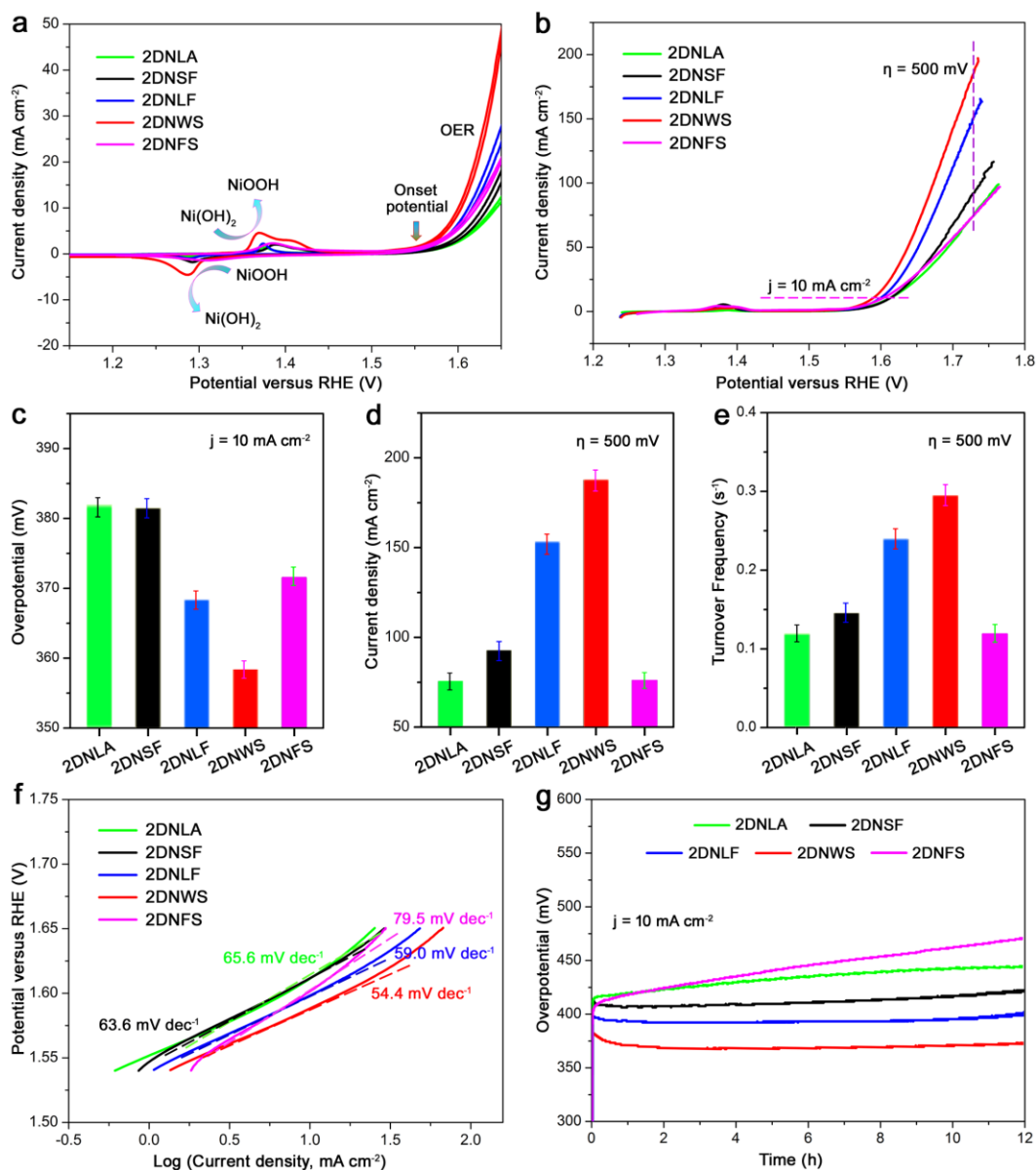


Figure 3. OER catalytic performance of Ni(OH)₂ with different architectures. (a) CV curves with a scan rate of 5 mV s⁻¹ in the voltage range of 1.22–1.72 V vs. RHE. (b) LSVs at a scan rate of 5 mV s⁻¹ in the voltage range of 1.22–1.92 V vs. RHE. (c) Overpotentials required to reach a current density of 10 mA cm⁻². (d) Current densities at an overpotential (η) of 500 mV. (e) TOFs calculated from current densities at an overpotential of 500 mV. (f) Tafel plots (potential *versus* log(current density)) derived from LSVs in the low overpotential region. (g) Chronopotentiometric responses recorded at a constant current density of 10 mA cm⁻² for 12 h.

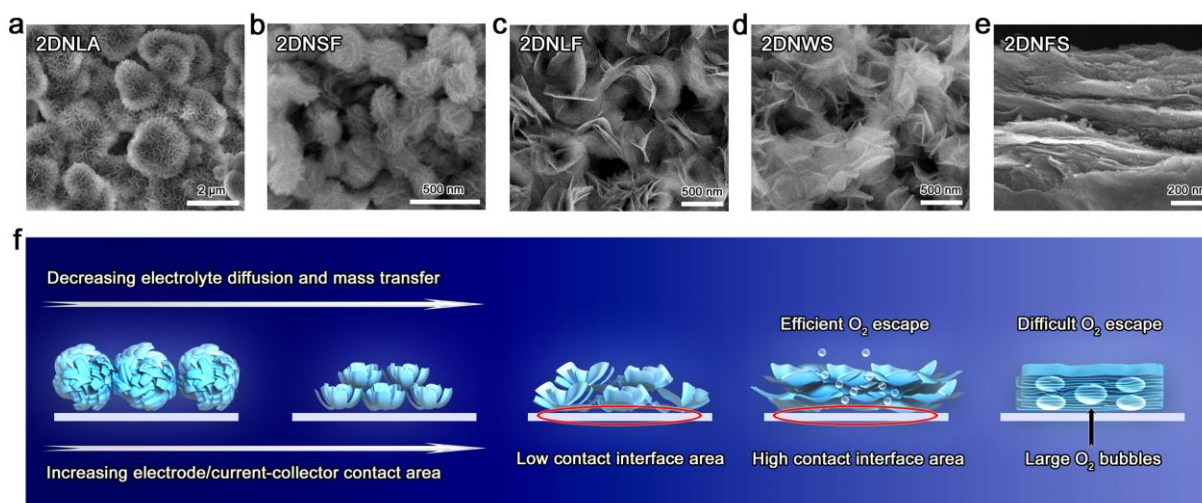


Figure 4. Effect of nanosheet architecture on OER catalytic performance. (a-e) Cross-sectional SEM images of different electrode films. (f) Schematic illustration showing the electrode-material/current-collector contact, electrolyte diffusion, and mass transfer (especially for O₂ escape) of electrode films constructed from different nanosheet architectures.

ASSOCIATED CONTENT

Supporting Information

The Supporting Information is available free of charge on the ACS Publications website at DOI:

Additional results

The authors declare no competing financial interest.

AUTHOR INFORMATION

Corresponding Author

*E-mail: shi@uow.edu.au.

*E-mail: p.liu@griffith.edu.au.

ORCID

ACKNOWLEDGMENTS

This work is financially supported by the Australian Research Council (ARC) Discovery Projects (DP160102627 and DP170104834), a ARC Discovery Early Career Researcher Award (DE170100607), the University of Wollongong—Beihang University (UOW-BUAA) Joint Research Centre. We also want to express our sincere gratitude to Prof. Huijun Zhao due to his strong support in the revision of this work in Griffith University.

REFERENCES

1. Xu, M.; Liang, T.; Shi, M.; Chen, H. Graphene-Like Two-Dimensional Materials. *Chem. Rev.* **2013**,

113, 3766—3798.

2. Tan, C.; Cao, X.; Wu, X.-J.; He, Q.; Yang, J.; Zhang, X.; Chen, J.; Zhao, W.; Han, S.; Nam, G.-H.; Sindoro, M.; Zhang, H. Recent Advances in Ultrathin Two-Dimensional Nanomaterials. *Chem. Rev.* **2017**, *117*, 6225—6331.
3. Sun, Y.; Gao, S.; Xie, Y. Atomically-Thick Two-Dimensional Crystals: Electronic Structure Regulation and Energy Device Construction. *Chem. Soc. Rev.* **2014**, *43*, 530—546.
4. Sun, Y.; Gao, S.; Lei, F.; Xiao, C.; Xie, Y. Ultrathin Two-Dimensional Inorganic Materials: New Opportunities for Solid State Nanochemistry. *Acc. Chem. Res.* **2015**, *48*, 3—12.
5. Zhang, X.; Xie, Y. Recent Advances in Free-Standing Two-Dimensional Crystals with Atomic Thickness: Design, Assembly and Transfer Strategies. *Chem. Soc. Rev.* **2013**, *42*, 8187—8199.
6. Weng, Q.; Wang, X.; Wang, X.; Bando, Y.; Golberg, D. Functionalized Hexagonal Boron Nitride Nanomaterials: Emerging Properties and Applications. *Chem. Soc. Rev.* **2016**, *45*, 3989—4012.
7. Lei, W.; Portehault, D.; Liu, D.; Qin, S.; Chen, Y. Porous Boron Nitride Nanosheets for Effective Water Cleaning. *Nat. Commun.* **2013**, *4*, 1777.
8. Yang, S.; Gong, Y.; Zhang, J.; Zhan, L.; Ma, L.; Fang, Z.; Vaitai, R.; Wang, X.; Ajayan, P. M. Exfoliated Graphitic Carbon Nitride Nanosheets as Efficient Catalysts for Hydrogen Evolution Under Visible Light. *Adv. Mater.* **2013**, *25*, 2452—2456.
9. Ye, M.-Y.; Zhao, Z.-H.; Hu, Z.-F.; Liu, L.-Q.; Ji, H.-M.; Shen, Z.-R.; Ma, T.-Y. 0D/2D Heterojunctions of Vanadate Quantum Dots/Graphitic Carbon Nitride Nanosheets for Enhanced Visible-Light-Driven Photocatalysis. *Angew. Chem. Int. Ed.* **2017**, *56*, 8407—8411.
10. Liu, H.; Du, Y.; Deng, Y.; Ye, P. D. Semiconducting Black Phosphorus: Synthesis, Transport Properties and Electronic Applications. *Chem. Soc. Rev.* **2015**, *44*, 2732—2743.
11. Li, L.; Yang, F.; Ye, G. J.; Zhang, Z.; Zhu, Z.; Lou, W.; Zhou, X.; Li, L.; Watanabe, K.; Taniguchi,

- T.; Chang, K.; Wang, Y.; Chen, X. H.; Zhang, Y. Quantum Hall Effect in Black Phosphorus Two-Dimensional Electron System. *Nat. Nanotech.* **2016**, *11*, 593—597.
12. Wang, Q.; O'Hare, D. Recent Advances in the Synthesis and Application of Layered Double Hydroxide (LDH) Nanosheets. *Chem. Rev.* **2012**, *112*, 4124—4155.
13. Yin, H.; Tang, Z. Ultrathin Two-Dimensional Layered Metal Hydroxides: An Emerging Platform for Advanced Catalysis, Energy Conversion and Storage. *Chem. Soc. Rev.* **2016**, *45*, 4873—4891.
14. Chhowalla, M.; Shin, H. S.; Eda, G.; Li, L.-J.; Loh, K. P.; Zhang, H. The Chemistry of Two-Dimensional Layered Transition Metal Dichalcogenide Nanosheets. *Nat. Chem.* **2013**, *5*, 263—275.
15. Lu, Q.; Yu, Y.; Ma, Q.; Chen, B.; Zhang, H. 2D Transition-Metal-Dichalcogenide-Nanosheet-Based Composites for Photocatalytic and Electrocatalytic Hydrogen Evolution Reactions. *Adv. Mater.* **2016**, *28*, 1917—1933.
16. Peng, Y.; Li, Y.; Ban, Y.; Jin, H.; Jiao, W.; Liu, X.; Yang, W. Metal-Organic Framework Nanosheets as Building Blocks for Molecular Sieving Membranes. *Science* **2014**, *346*, 1356—1359.
17. Wang, Y.; Zhao, M.; Ping, J.; Chen, B.; Cao, X.; Huang, Y.; Tan, C.; Ma, Q.; Wu, S.; Yu, Y.; Lu, Q.; Chen, J.; Zhao, W.; Ying, Y.; Zhang, H. Bioinspired Design of Ultrathin 2D Bimetallic Metal-Organic-Framework Nanosheets Used as Biomimetic Enzymes. *Adv. Mater.* **2016**, *28*, 4149—4155.
18. Colson, J. W.; Woll, A. R.; Mukherjee, A.; Levendorf, M. P.; Spitler, E. L.; Shields, V. B.; Spencer, M. G.; Park, J.; Dichtel, W. R. Oriented 2D Covalent Organic Framework Thin Films on Single-Layer Graphene. *Science* **2011**, *332*, 228—231.
19. Wang, S.; Wang, Q.; Shao, P.; Han, Y.; Gao, X.; Ma, L.; Yuan, S.; Ma, X.; Zhou, J.; Feng, X.; Wang, B. Exfoliation of Covalent Organic Frameworks into Few-Layer Redox-Active Nanosheets as Cathode Materials for Lithium-Ion Batteries. *J. Am. Chem. Soc.* **2017**, *139*, 4258—4261.
20. Anasori, B.; Xie, Y.; Beidaghi, M.; Lu, J.; Hosler, B. C.; Hultman, L.; Kent, P. R. C.; Gogotsi, Y.;

- Barsoum, M. W. Two-Dimensional, Ordered, Double Transition Metals Carbides (MXenes). *ACS Nano* **2015**, *9*, 9507—9516.
21. Ding, L.; Wei, Y.; Wang, Y.; Chen, H.; Caro, J.; Wang, H. A Two-Dimensional Lamellar Membrane: MXene Nanosheet Stacks. *Angew. Chem. Int. Ed.* **2017**, *56*, 1825—1829.
22. Nicolosi, V.; Chhowalla, M.; Kanatzidis, M. G.; Strano, M. S.; Coleman, J. N. Liquid Exfoliation of Layered Materials. *Science* **2013**, *340*, 1226419.
23. Huang, X.; Zeng, Z.; Zhang, H. Metal Dichalcogenide Nanosheets: Preparation, Properties and Applications. *Chem. Soc. Rev.* **2013**, *42*, 1934—1946.
24. Tan, C.; Zhang, H. Wet-Chemical Synthesis and Applications of Non-Layer Structured Two-Dimensional Nanomaterials. *Nat. Commun.* **2015**, *6*, 7873.
25. Wang, F.; Wang, Z.; Shifa, T. A.; Wen, Y.; Wang, F.; Zhan, X.; Wang, Q.; Xu, K.; Huang, Y.; Yin, L.; Jiang, C.; He, J. Two-Dimensional Non-Layered Materials: Synthesis, Properties and Applications. *Adv. Funct. Mater.* **2017**, *27*, 1603254.
26. Wang, Q. H.; Kalantar-Zadeh, K.; Kis, A.; Coleman, J. N.; Strano, M. S. Electronics and Optoelectronics of Two-Dimensional Transition Metal Dichalcogenides. *Nat. Nanotech.* **2012**, *7*, 699—712.
27. Sun, Y.; Gao, S.; Lei, F.; Xie, Y. Atomically-Thin Two-Dimensional Sheets for Understanding Active Sites in Catalysis. *Chem. Soc. Rev.* **2015**, *44*, 623—636.
28. Cao, X.; Tan, C.; Zhang, X.; Zhao, W.; Zhang, H. Solution-Processed Two-Dimensional Metal Dichalcogenide-Based Nanomaterials for Energy Storage and Conversion. *Adv. Mater.* **2016**, *28*, 6167—6197.
29. Dou, Y.; Zhang, L.; Xu, X.; Sun, Z.; Liao, T.; Dou, S. X. Atomically Thin Non-Layered Nanomaterials for Energy Storage and Conversion. *Chem. Soc. Rev.* **2017**, *46*, 7338—7373.

30. Dou, Y.; Liao, T.; Ma, Z.; Tian, D.; Liu, Q.; Xiao, F.; Sun, Z.; Kim, J. H.; Dou, S. X. Graphene-Like Holey Co_3O_4 Nanosheets as a Highly Efficient Catalyst for Oxygen Evolution Reaction. *Nano Energy* **2016**, *30*, 267—275.
31. Sun, Y.; Lei, F.; Gao, S.; Pan, B.; Zhou, J.; Xie, Y. Atomically Thin Dioxide Sheets for Efficient Catalytic Oxidation of Carbon Monoxide. *Angew. Chem. Int. Ed.* **2013**, *52*, 10569—10572.
32. Sun, Y.; Liu, Q.; Gao, S.; Cheng, H.; Lei, F.; Sun, Z.; Jiang, Y.; Su, H.; Wei, Q.; Xie, Y. Pits Confined in Ultrathin Cerium(IV) Oxide for Studying Catalytic Centers in Carbon Monoxide Oxidation. *Nat. Commun.* **2013**, *4*, 2899.
33. Sun, Y.; Gao, S.; Lei, F.; Liu, J.; Liang, L.; Xie, Y. Atomically-Thin Non-Layered Cobalt Oxide Porous Sheets for Highly Efficient Oxygen-Evolving Electrocatalysts. *Chem. Sci.* **2014**, *5*, 3976—3982.
34. Liu, Y.; Xiao, C.; Li, Z.; Liu, Y. Vacancy Engineering for Tuning Electron and Phonon Structures of Two-Dimensional Materials. *Adv. Energy Mater.* **2016**, *6*, 1600436.
35. Gao, S.; Sun, Z.; Liu, W.; Jiao, X.; Zu, X.; Hu, Q.; Sun, Y.; Yao, T.; Zhang, W.; Wei, S.; Xie, Y. Atomic Layer Confined Vacancies for Atomic-Level Insights into Carbon Dioxide Electroreduction. *Nat. Commun.* **2017**, *8*, 14503.
36. Liu, Y.; Hua, X.; Xiao, C.; Zhou, T.; Huang, P.; Guo, Z.; Pan, B.; Xie, Y. Heterogeneous Spin States in Ultrathin Nanosheets Induce Subtle Lattice Distortion To Trigger Efficient Hydrogen Evolution. *J. Am. Chem. Soc.* **2016**, *138*, 5087—5092.
37. Lei, F.; Zhang, L.; Sun, Y.; Liang, L.; Liu, K.; Xu, J.; Zhang, Q.; Pan, B.; Luo, Y.; Xie, Y. Atomic-Layer-Confined Doping for Atomic-Level Insights into Visible-Light Water Splitting. *Angew. Chem. Int. Ed.* **2015**, *54*, 9266—9270.
38. Dou, Y.; Xu, J.; Ruan, B.; Liu, Q.; Pan, Y.; Sun, Z.; Dou, S. X. Atomic Layer-by-Layer

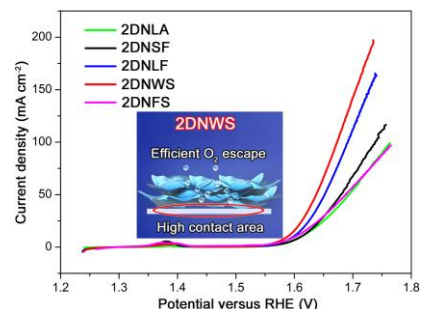
- Co₃O₄/Graphene Composite for High Performance Lithium-Ion Batteries. *Adv. Energy Mater.* **2016**, 6, 1501835.
39. Lei, F.; Liu, W.; Sun, Y.; Xu, J.; Liu, K.; Liang, L.; Yao, T.; Pan, B.; Wei, S.; Xie, Y. Metallic Tin Quantum Sheets Confined in Graphene Toward High-Efficiency Carbon Dioxide Electroreduction. *Nat. Commun.* **2016**, 7, 12697.
40. Yang, W.; Zhang, X.; Xie, Y. Advances and Challenges in Chemistry of Two-Dimensional Nanosheets. *Nano Today* **2016**, 11, 793—816.
41. Deng, D.; Novoselov, K. S.; Fu, Q.; Zheng, N.; Tian, Z.; Bao, X. Catalysis with Two-Dimensional Materials and Their Heterostructures. *Nat. Nanotech.* **2016**, 11, 218—230.
42. Lin, Z.; Carvalho, B. R.; Kahn, E.; Lv, R.; Rao, R.; Terrones, H.; Pimenta, M. A.; Terrones, M. Defect Engineering of Two-Dimensional Transition Metal Dichalcogenides. *2D Mater.* **2016**, 3, 022002.
43. Colonna, S.; Monticelli, O.; Gomez, J.; Novara, C.; Saracco, G.; Fina, A. Effect of Morphology and Defectiveness of Graphene-Related Materials on the Electrical and Thermal Conductivity of Their Polymer Nanocomposites. *Polymer* **2016**, 102, 292—300.
44. Gong, Y.; Yang, S.; Zhan, L.; Ma, L.; Vajtai, R.; Ajayan, P. M. A Bottom-Up Approach to Build 3D Architectures from Nanosheets for Superior Lithium Storage. *Adv. Funct. Mater.* **2014**, 24, 125—130.
45. Li, H.; Wang, X. Three-Dimensional Architectures Constructed Using Two-Dimensional Nanosheets. *Sci. China Chem.* **2015**, 58, 1792—1799.
46. Sun, Z.; Liao, T.; Dou, Y.; Hwang, S. M.; Park, M.-S.; Jiang, L.; Kim, J. H.; Dou, S. X. Generalized Self-Assembly of Scalable Two-Dimensional Transition Metal Oxide Nanosheets. *Nat. Commun.* **2014**, 5, 3813.

47. Sun, Z.; Kim, J. H.; Zhao, Y.; Bijarbooneh, F.; Malhras, V.; Lee, Y.; Kang, Y.-M.; Dou, S. X. Rational Design of 3D Dendritic TiO₂ Nanostructures with Favorable Architectures. *J. Am. Chem. Soc.* **2011**, *133*, 19314—19317.
48. Christensen, G.; Younes, H.; Hong, H.; Smith, P. Effects of Solvent Hydrogen Bonding, Viscosity, and Polarity on the Dispersion and Alignment of Nanofluids Containing Fe₂O₃ Nanoparticles. *J. Appl. Phys.* **2015**, *118*, 214302.
49. Gao, M.; Sheng, W.; Zhuang, Z.; Fang, Q.; Gu, S.; Jiang, J.; Yan, Y. Efficient Water Oxidation Using Nanostructured α -Nickel-Hydroxide as an Electrocatalyst. *J. Am. Chem. Soc.* **2014**, *136*, 7077—7084.
50. Tkalych, A. J.; Yu, K.; Carter, E. A. Structural and Electronic Features of β -Ni(OH)₂ and β -NiOOH from First Principles. *J. Phys. Chem. C* **2015**, *119*, 24315—24322.
51. Liu, Z.; Ma, R.; Osada, M.; Takada, K.; Sasaki, T. Selective and Controlled Synthesis of α - and β -Cobalt Hydroxides in Highly Developed Hexagonal Platelets. *J. Am. Chem. Soc.* **2005**, *127*, 13869—13874.
52. Wang, J.-G.; Jin, D.; Zhou, R.; Li, X.; Liu, X.-r.; Shen, C.; Xie, K.; Li, B.; Kang, F.; Wei, B. Highly Flexible Graphene/Mn₃O₄ Nanocomposite Membrane as Advanced Anodes for Li-Ion Batteries. *ACS Nano* **2016**, *10*, 6227—6234.
53. Cao, K.; Jiao, L.; Xu, H.; Liu, H.; Kang, H.; Zhao, Y.; Liu, Y.; Wang, Y.; Yuan, H. Reconstruction of Mini-Hollow Polyhedron Mn₂O₃ Derived from MOFs as a High-Performance Lithium Anode Material. *Adv. Sci.* **2016**, *3*, 1500185.
54. Xu, Z. W.; Ngan, A. H. W. TEM Study of Electron Beam-Induced Crystallization of Amorphous GeSi Films. *Phil. Mag. Lett.* **2004**, *84*, 719—728.
55. Klaus, S.; Cai, Y.; Louie, M. W.; Trotochaud, L.; Bell, A. T. Effects of Fe Electrolyte Impurities on

- Ni(OH)₂/NiOOH Structure and Oxygen Evolution Activity. *J. Phys. Chem. C* **2015**, *119*, 7243—7254.
56. Friebe, D.; Louie, M. W.; Bajdich, M.; Sanwald, K. E.; Cai, Y.; Wise, A. M.; Cheng, M.-J.; Sokaras, D.; Weng, T.-C.; Alonso-Mori, R.; Davis, R. C.; Bargar, J. R.; Norskov, J. K.; Nilsson, A.; Bell, A. T. Identification of Highly Active Fe Sites in (Ni,Fe)OOH for Electrocatalytic Water Splitting. *J. Am. Chem. Soc.* **2015**, *137*, 1305—1313.
 57. Bediako, D. K.; Lassalle-Kaiser, B.; Surendranath, Y.; Yano, J.; Yachandra, V. K.; Nocera, D. G. Structure-Activity Correlations in a Nickel-Borate Oxygen Evolution Catalyst. *J. Am. Chem. Soc.* **2012**, *134*, 6801—6809.
 58. Shinagawa, T.; Ng, M. T.-K.; Takanabe, K. Boosting the Performance of the Nickel Anode in the Oxygen Evolution Reaction by Simple Electrochemical Activation. *Angew. Chem.* **2017**, *129*, 5143—5147.
 59. Lu, Z.; Wang, H.; Kong, D.; Yan, K.; Hsu, P.-C.; Zheng, G.; Yao, H.; Liang, Z.; Sun, X.; Cui, Y. Electrochemical Tuning of Layered Lithium Transition Metal Oxides for Improvement of Oxygen Evolution Reaction. *Nat. Commun.* **2014**, *5*, 4345.
 60. Seitz, L. C.; Dickens, C. F.; Nishio, K.; Hikita, Y.; Montoya, J.; Doyle, A.; Kirk, C.; Vojvodie, A.; Hwang, H. Y.; Norskov, J. K.; Jaramillo, T. F. A Highly Active and Stable IrO_x/SrIrO₃ Catalyst for Oxygen Evolution Reaction. *Science* **2016**, *353*, 1011—1014.
 61. Xu, X.; Song, F.; Hu, X. A Nickel Iron Diselenide-Derived Efficient Oxygen-Evolution Catalyst. *Nat. Commun.* **2016**, *7*, 12324.
 62. Zhang, W.; Qi, J.; Liu, K.; Cao, R. A Nickel-Based Integrated Electrode from an Autologous Growth Strategy for Highly Efficient Water Oxidation. *Adv. Energy Mater.* **2016**, *6*, 1502489.
 63. Bae, S.-H.; Kim, J.-E.; Randriamahazaka, H.; Moon, S.-Y.; Park, J.-Y.; Oh, I.-K. Seamlessly

- Conductive 3D Nanoarchitecture of Core-Shell Ni-Co Nanowire Network for Highly Efficient Oxygen Evolution. *Adv. Energy Mater.* **2017**, 7, 1601492.
64. Song, F.; Hu, X. Ultrathin Cobalt-Manganese Layered Double Hydroxide Is an Efficient Oxygen Evolution Catalyst. *J. Am. Chem. Soc.* **2014**, 136, 16481—16484.
65. Smith, R. D. L.; Berlinguette, C. P. Accounting for the Dynamic Oxidative Behavior of Nickel Anodes. *J. Am. Chem. Soc.* **2016**, 138, 1561—1567.
66. Conesa, J. C. Electronic Structure of the (Undoped and Fe-Doped) NiOOH O₂ Evolution Electrocatalyst. *J. Phys. Chem. C* **2016**, 120, 18999—19010.
67. Trotochaud, L.; Young, S. L.; Ranney, J. K.; Boettcher, S. W. Nickel-Iron Oxyhydroxide Oxygen-Evolution Electrocatalysts: The Role of Intentional and Incidental Iron Incorporation. *J. Am. Soc. Soc.* **2014**, 136, 6744—6753.
68. Duan, J.; Chen, S.; Vasileff, A.; Qiao, S. Z. Anion and Cation Modulation in Metal Compounds for Bifunctional Overall Water Splitting. *ACS Nano* **2016**, 10, 8738—8745.

GRAPHICAL TABLE OF CONTENTS



The effect of nanosheet architecture of atomically thin transition metal (hydr)oxide on OER catalysis is investigated. The results demonstrate the obvious superiority of wrinkled nanosheets in both catalytic activity and durability. The excellent performance is mainly attributable to the 3D porous electrode structure, which not only provides sufficient electrode-material/current-collector contact, but also enables facile electrolyte diffusion and efficient O₂ escape.

Supporting Information

Manipulating the Architecture of Atomically Thin Transition Metal (Hydr)oxides for Enhanced Oxygen Evolution Catalysis

Yuhai Dou,^{†,‡} Lei Zhang,[†] Jiantie Xu,[†] Chun-Ting He,[‡] Xun Xu,[†] Ziqi Sun,[§] Ting Liao,[§] Balázs Nagy,[‡] Porun Liu,^{*,‡} and Shi Xue Dou^{*,†}

[†]Institute for Superconducting and Electronic Materials, Australian Institute for Innovative Materials, University of Wollongong, Wollongong, New South Wales 2500, Australia

[‡]Centre for Clean Environment and Energy, Gold Coast Campus, Griffith University, Gold Coast, Queensland 4222, Australia

[§]School of Chemistry, Physics and Mechanical Engineering, Queensland University of Technology, Brisbane, Queensland 4000, Australia

*Corresponding Authors. E-mail: shi@uow.edu.au; p.liu@griffith.edu.au

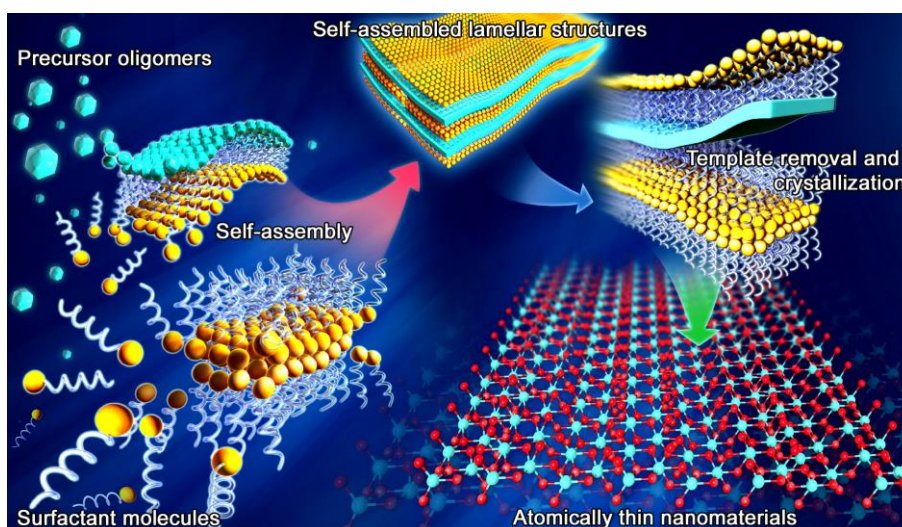


Figure S1 Bottom-up self-assembly synthesis of atomically thin nanomaterials. The figure is reproduced with permission from Ref. 1, Copyright 2014 Nature Publishing Group.

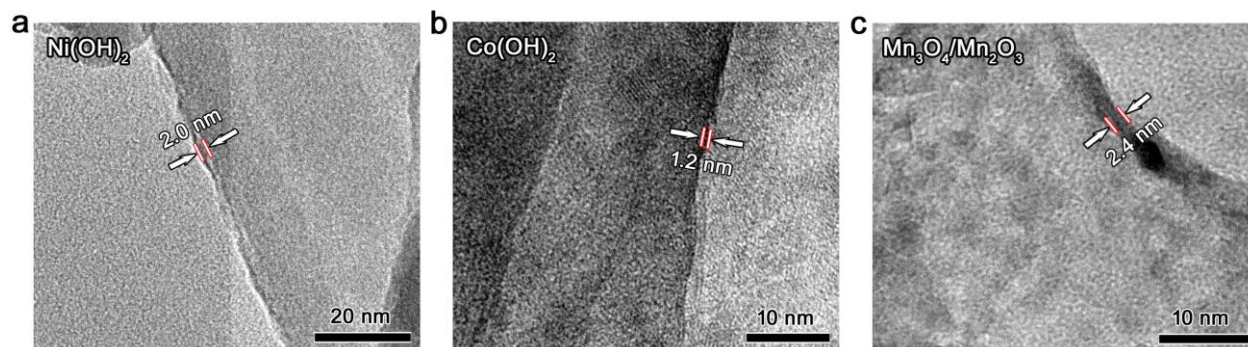


Figure S2 HRTEM images of cross sections of atomically thin transition metal hydroxides. (a) $\text{Ni}(\text{OH})_2$. (b) $\text{Co}(\text{OH})_2$. (c) $\text{Mn}_3\text{O}_4/\text{Mn}_2\text{O}_3$. The thicknesses of the nanosheets are 2.0, 1.2, and 2.4 nm, respectively.

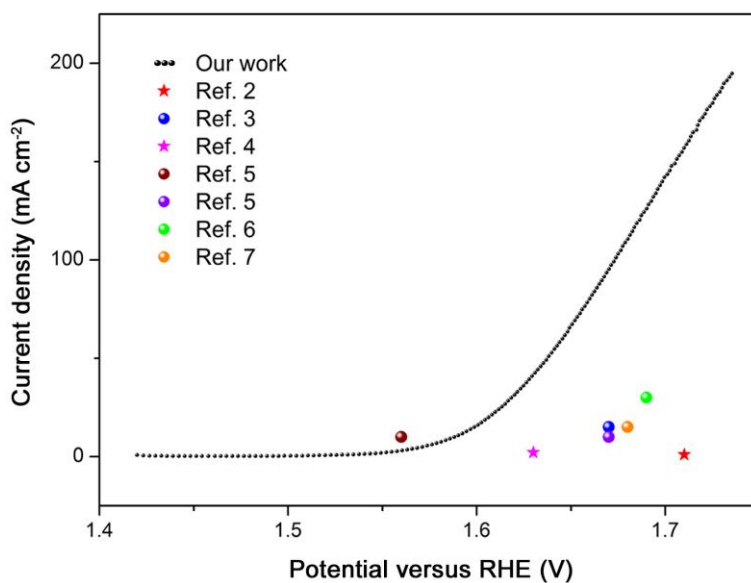


Figure S3 Comparison of catalytic performance between $\text{Ni}(\text{OH})_2$ wrinkled nanosheets (2DNWS) and previously reported $\text{Ni}(\text{OH})_2$ catalysts.²⁻⁷ Balls stand for results tested in 0.1 M KOH and stars stand for those in 1 M KOH.

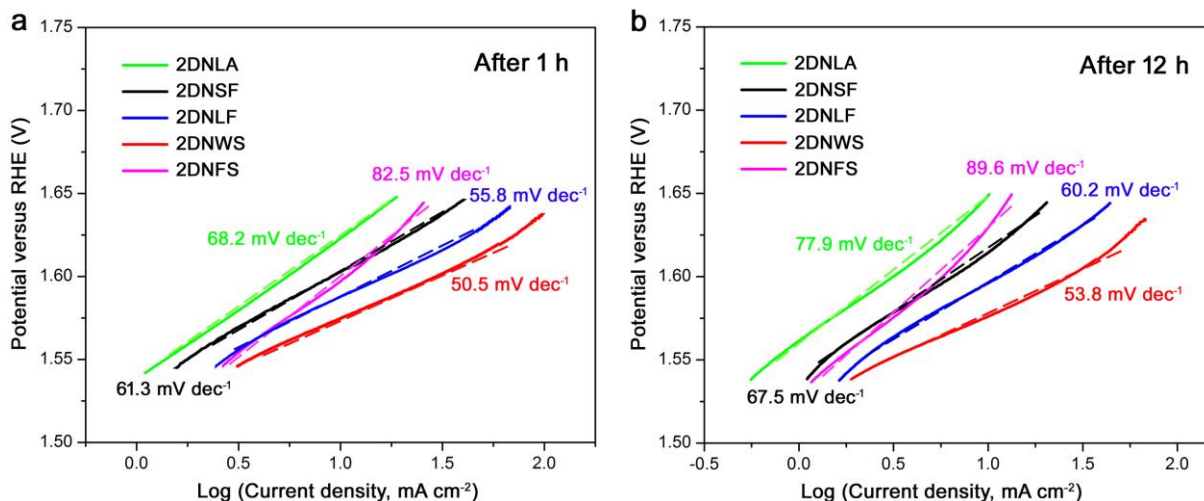


Figure S4 Tafel plots after 1 h and 12 h durability tests. (a) After 1 h chronopotentiometric test. (b) After 12 h chronopotentiometric test.

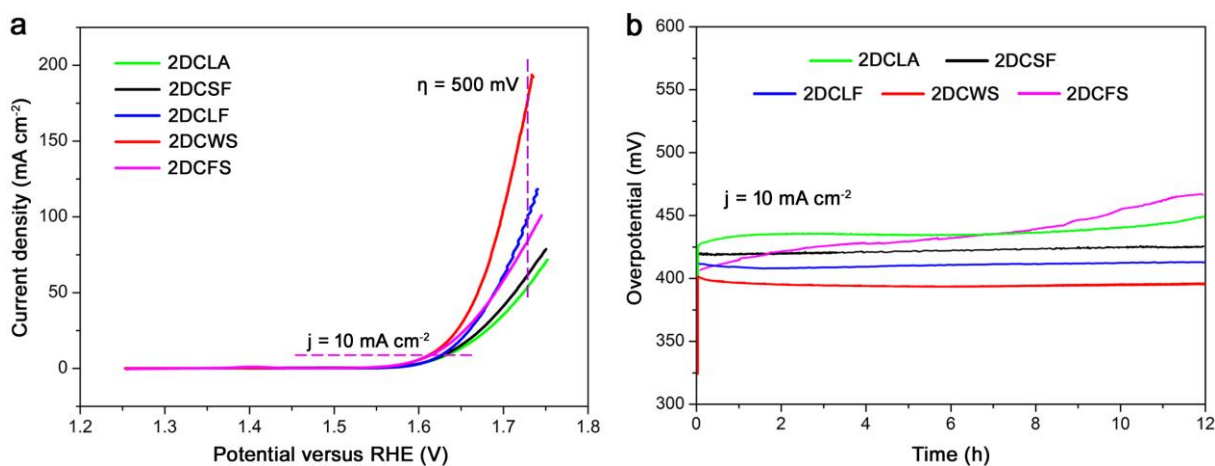


Figure S5 OER catalytic performance of Co(OH)₂ with different architectures. (a) LSVs at a scan rate of 5 mV s⁻¹ in the voltage range of 1.22–1.92 V vs. RHE. (b) Chronopotentiometric responses recorded at a constant current density of 10 mA cm⁻² for 12 h.

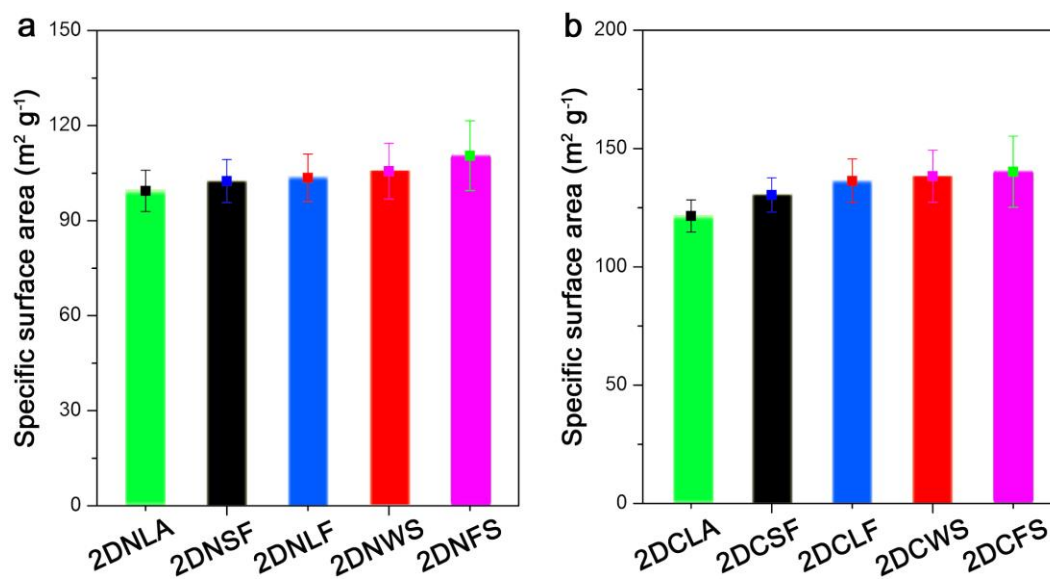


Figure S6 BET surface areas of Ni(OH)_2 and Co(OH)_2 with different nanosheet architectures. (a) Ni(OH)_2 . (b) Co(OH)_2 .

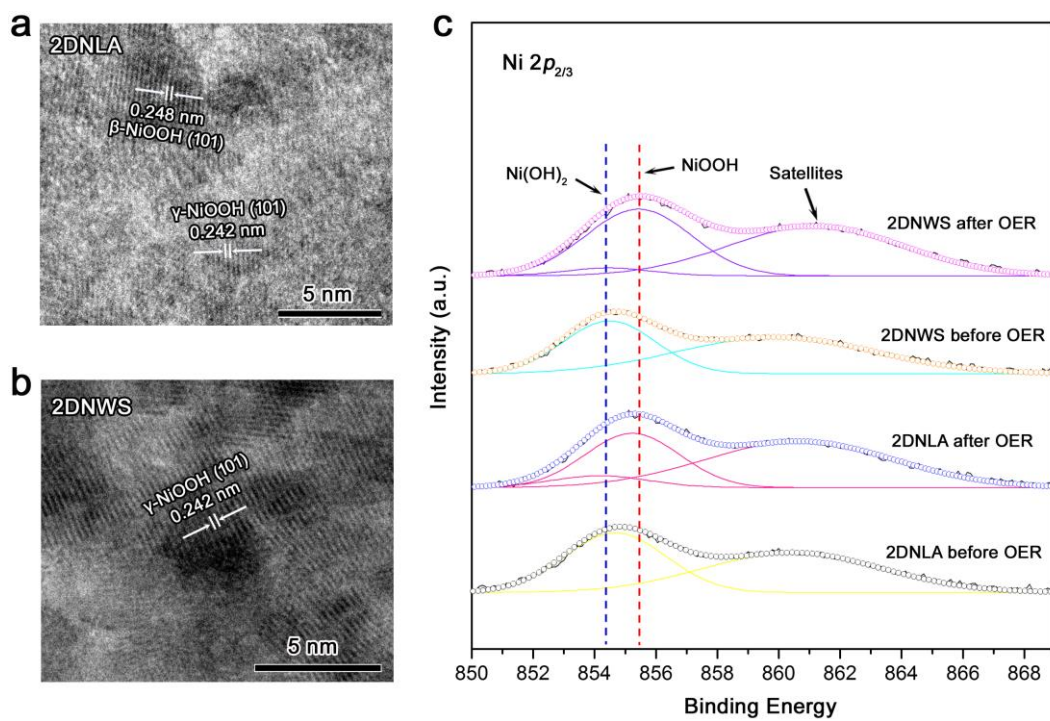


Figure S7 HRTEM images and $\text{Ni } 2p_{2/3}$ XPS spectra of 2DNLA and 2DNWS after OER test. (a) HRTEM images of 2DNLA and 2DNWS. (c) $\text{Ni } 2p_{2/3}$ XPS spectra.

HRTEM image of 2DNLA after OER test. (b) HRTEM image of 2DNWS after OER test. (c) Ni 2p_{2/3} XPS spectra of 2DNLA and 2DNWS before and after OER test.

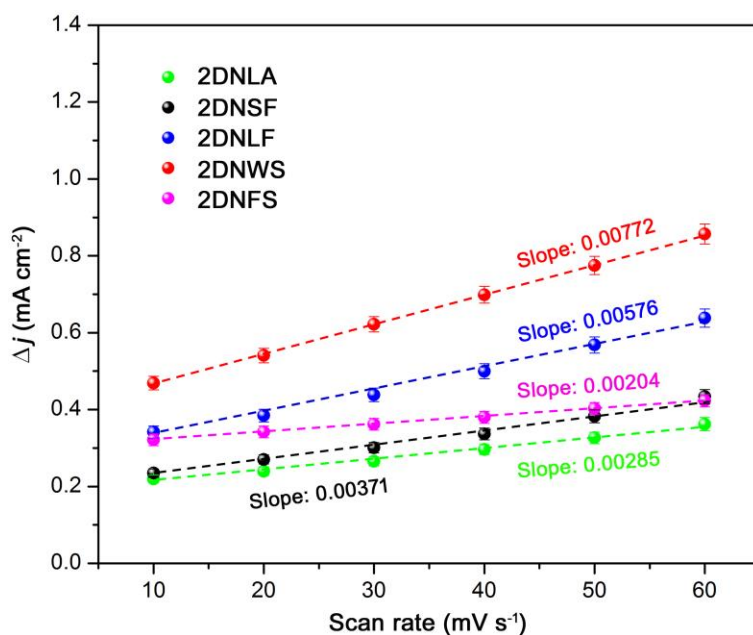


Figure S8 The differences in current density ($\Delta j = j_{\text{anode}} - j_{\text{cathode}}$) at 1.273 V vs. RHE plotted against scan rates. The slope is twice the double-layer capacitance (Cdl).

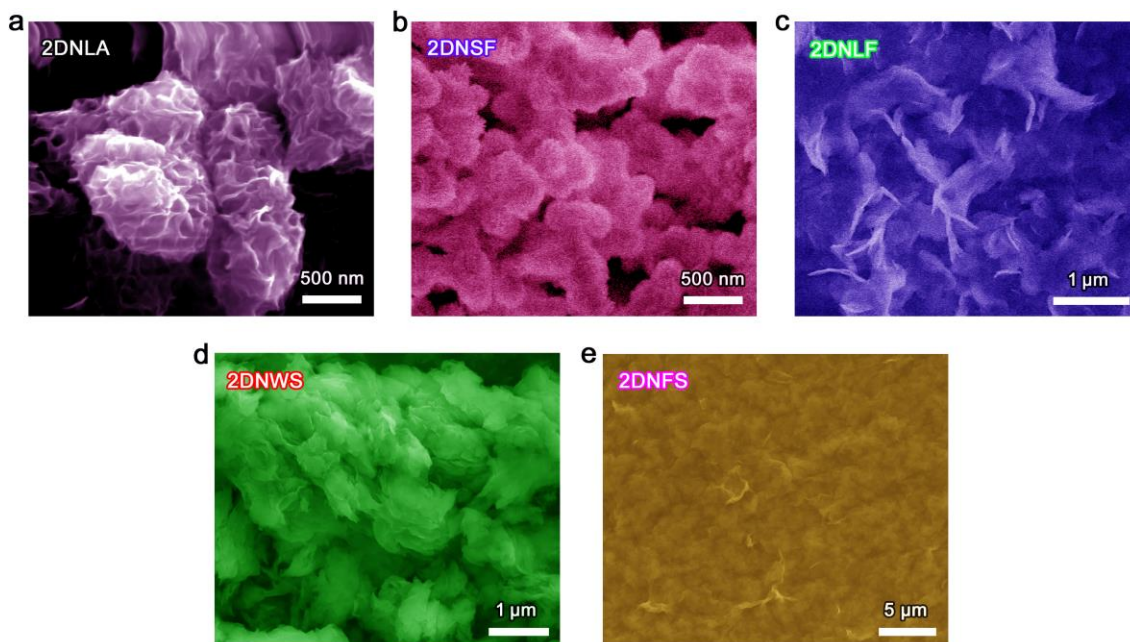


Figure S9 SEM images of different Ni(OH)₂ architectures after 12 h chronopotentiometric test. (a) 2DNLA. (b) 2DNSF. (c) 2DNLF. (d) 2DNWS. (e) 2DNFS.

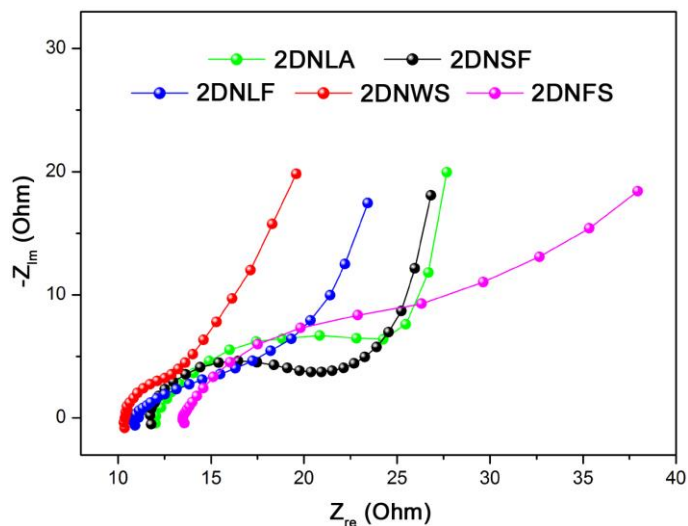


Figure S10 Nyquist plots of different Ni(OH)₂ architectures after 12 h chronopotentiometric test.

Table S1 Compositions of the precursor solutions for atomically thin transition metal hydroxides with different architectures. (NO.1-5 represent 2DXLA, 2DXSF, 2DXLF, 2DXWS, and 2DXFS, respectively)

Chemicals	Ni(OH) ₂					Co(OH) ₂					Mn ₃ O ₄ /Mn ₂ O ₃				
	NO.1	NO.2	NO.3	NO.4	NO.5	NO.1	NO.2	NO.3	NO.4	NO.5	NO.1	NO.2	NO.3	NO.4	NO.5
Acetone, g	3.00														
Ethanol, g											3.00				
P123, g						0.20									
EG, ml						12.00									
H ₂ O, ml	0.00	0.50	2.00	8.00	15.00	0.00	0.50	1.00	8.00	15.00	0.00	0.50	2.00	4.00	10.00
H ₂ O/EG, vol%	0.00	0.04	0.17	0.67	1.25	0.00	0.04	0.08	0.67	1.25	0.00	0.04	0.17	0.33	0.83
Ni(Ac) ₂ ·4H ₂ O, g	0.12														

Co(Ac)₂· 4H₂O, g		0.13	
Mn(Ac)₂· 4H₂O, g			0.25
HMTA, g	0.07	0.07	0.14

Table S2 Interlayer distance of Ni(OH)₂ nanosheets with different architectures. (The data was calculated from XRD spectra)

Architecture	2DNLA	2DNSF	2DNLF	2DNWS	2DNFS
H₂O addition, g	0.00	0.50	2.00	8.00	15.00
Phase	β -/ α -Ni(OH) ₂	β -/ α -Ni(OH) ₂	α -Ni(OH) ₂	α -Ni(OH) ₂	α -Ni(OH) ₂
Plan	(001) of β	(001) of β	(003)	(003)	(003)
2θ, °	10.19	10.12	5.94	5.74	5.68
d_{00n}, Å	4.35	4.38	7.44	7.70	7.80

References

1. Sun, Z.; Liao, T.; Dou, Y.; Hwang, S. M.; Park, M.-S.; Jiang, L.; Kim, J. H.; Dou, S. X. Generalized Self-Assembly of Scalable Two-Dimensional Transition Metal Oxide Nanosheets. *Nat. Commun.* **2014**, *5*, 3813.
2. Trotochaud, L.; Young, S. L.; Ranney, J. K.; Boettcher, S. W. Nickel-Iron Oxyhydroxide Oxygen-Evolution Electrocatalysts: The Role of Intentional and Incident Iron Incorporation. *J. Am. Chem. Soc.* **2014**, *136*, 6744—6753.
3. Zhu, K.; Liu, H.; Li, M.; Wang, J.; Zhu, X.; Yang, W. Atomic-Scale Topochemical Preparation of Crystalline Fe³⁺-Doped β -Ni(OH)₂ for Ultrahigh-Rate Oxygen Evolution Reaction. *J. Mater. Chem. A* **2017**, *5*, 7753—7758.
4. Nai, J.; Yin, H.; You, T.; Zheng, L.; Zhang, J.; Wang, P.; Jin, Z.; Tian, Y.; Liu, J.; Tang, Z.; Guo, L. Efficient Electrocatalytic Water Oxidation by Using Amorphous Ni-Co Double Hydroxides Nanocages. *Adv. Energy Mater.* **2015**, *5*, 1401880.
5. Gao, M.; Sheng, W.; Zhuang, Z.; Fang, Q.; Gu, S.; Jiang, J.; Yan, Y. Efficient Water Oxidation Using Nanostructured α -Nickel-Hydroxide as an Electrocatalyst. *J. Am. Chem. Soc.* **2014**, *136*, 7077—7084.
6. Chen, J. Y. C.; Dang, L.; Liang, H.; Bi, W.; Gerken, J. B.; Jin, S.; Alp, E. E.; Stahl, S. S. Operando Analysis of NiFe and Fe Oxyhydroxide Electrocatalysts for Water Oxidation: Detection of Fe⁴⁺ by Mossbauer Spectroscopy. *J. Am. Chem. Soc.* **2015**, *137*, 15090—15093.

7. Gorlin, M.; Chernev, P.; Araujo, J. F. d.; Reier, T.; Dresp, S.; Paul, B.; Krahner, R.; Dau, H.; Strasser, P. Oxygen Evolution Reaction Dynamics, Faradaic Charge Efficiency, and the Active Metal Redox States of Ni-Fe Oxide Water Splitting Electrocatalysts. *J. Am. Chem. Soc.* **2016**, *138*, 5603—5614.